2-6-2019

On the Broad-Band Synchrotron Spectra of Pulsar Wind Nebulae

Siyao Xu
University of Wisconsin, sxu93@wisc.edu

Noel Klinger
The George Washington University, noelklingler@email.gwu.edu

Oleg Kargaltsev
The George Washington University, kargaltsev@email.gwu.edu

Bing Zhang
University of Nevada, Las Vegas, bing.zhang@unlv.edu

The Astrophysical Journal, 872:10 (10pp), 2019 February 10 https://doi.org/10.3847/1538-4357/aafb2e

On the Broadband Synchrotron Spectra of Pulsar Wind Nebulae

Siyao Xu[1,4], Noel Klingler[2], Oleg Kargaltsev[2], and Bing Zhang[3]
[1] Department of Astronomy, University of Wisconsin, 475 North Charter Street, Madison, WI 53706, USA; sxu93@wisc.edu
[2] Department of Physics, The George Washington University, 725 21st Street NW, Washington, DC 20052, USA; noelklingler@email.gwu.edu, kargaltsev@email.gwu.edu
[3] Department of Physics and Astronomy, University of Nevada Las Vegas, NV 89154, USA; zhang@physics.unlv.edu
Received 2018 November 8; revised 2018 December 26; accepted 2018 December 27; published 2019 February 6

Abstract

As shown by broadband observations, pulsar wind nebulae (PWNe) are characterized by a broken power-law spectrum of synchrotron emission. Based on modern magnetohydrodynamic (MHD) turbulence theories, we investigate the reacceleration of electrons in the PWN through the adiabatic stochastic acceleration (ASA), which arises from fundamental dynamics of MHD turbulence. The ASA acts to flatten the injected energy spectrum of electrons at low energies, while synchrotron cooling results in a steep spectrum of electrons at high energies. Their dominance in different energy ranges leads to a flat radio spectrum (F_ν) and a steep X-ray spectrum. Our analytical spectral shapes generally agree well with the observed synchrotron spectra of radio- and X-ray-bright PWNe. The spectral break corresponding to the balance between the ASA and synchrotron losses provides a constraint on the acceleration timescale of the ASA and the magnetic field strength in the PWN.

Key words: acceleration of particles – pulsars: general – radiation mechanisms: non-thermal – turbulence

1. Introduction

Poynting-flux-dominated pulsar winds (PWs) and their surrounding pulsar wind nebulae (PWNe) serve as a representative example for studying the mechanisms of energy dissipation and particle acceleration in high-energy astrophysical environments. Broadband observations reveal a broken power law consisting of a flat radio spectrum (F_ν) and a steeper X-ray spectrum as a characteristic radiation spectrum of PWNe (e.g.,Chevalier 2005; Gaensler & Slane 2006; Reynolds et al. 2017). Although the multiwavelength radiation is believed to be synchrotron in radio and X-rays, the broadband spectral shape is not well understood.

The stochastic nature of turbulent magnetic fields is frequently invoked to model the flat spectrum F_ν of radio emission (e.g., Fleishman & Bietenholz 2007; Tanaka & Asano 2017). Turbulent magnetic fields in PWNe are naturally expected and also indicated by observations (Reynolds & Aller 1988; Yusef-Zadeh & Gaensler 2005; Moran et al. 2013; Ma et al. 2016) and simulations (Porth et al. 2014b). Magnetohydrodynamic (MHD) turbulence is a highly nonlinear problem. Recent theoretical studies (Goldreich & Sridhar 1995; Lazarian & Vishniac 1999, hereafter LV99) offer new insights into its nonlinear dynamics. This nonlinear character cannot be captured by a superposition of linear waves, which was traditionally assumed for modeling MHD turbulence (Giacalone & Jokipii 1999). The updated understanding of fundamental properties of MHD turbulence brings paradigm changes in studying important physical processes, e.g., magnetic reconnection and dissipation (LV99; Zhang & Yan 2011; Deng et al. 2015; Lazarian et al. 2018), particle acceleration, and radiation (Pohl et al. 2005; Brunetti & Lazarian 2007; Yan et al. 2008; Xu et al. 2016, 2018; Guo et al. 2017; Xu & Zhang 2017; Xu & Lazarian 2018), related to high-energy astrophysical phenomena.

Alfvén modes dominate the dynamics of MHD turbulence and carry the majority of turbulent kinetic energy (Cho & Lazarian 2003). The anisotropic scaling of Alfvénic turbulence in the frame of the *local* magnetic field (LV99) is a direct consequence of its nonlinear dynamics. Due to the turbulence anisotropy, the stochastic particle acceleration via gyroresonance with Alfvénic turbulence is inefficient (Chandran 2000; Yan & Lazarian 2002). For relativistic particles that undergo inefficient gyroresonance scattering, a new acceleration mechanism arising from the basic dynamics of Alfvénic turbulence is applicable (Brunetti & Lazarian 2016). The stochastic dynamo stretching and reconnection shrinking of turbulent magnetic fields lead to a globally diffusive acceleration of particles entrained on field lines. Systematic energy change of particles during the trapping in individual turbulent eddies makes the acceleration highly efficient. Xu & Zhang (2017) and Xu et al. (2018) term it as "adiabatic stochastic acceleration (ASA)" to distinguish it from the non-ASA through gyroresonance scattering and apply it to interpreting the Band function spectrum commonly observed in gamma-ray bursts (GRBs; Band et al. 1993; Preece et al. 2000). The ASA- and synchrotron cooling-dominated electron energy distributions explain well the hard low-energy spectrum and softer high-energy spectrum of GRB prompt emission, respectively. As the ASA is generally applicable to particle acceleration in turbulent magnetic fields, here we introduce the ASA and examine its effect, together with synchrotron cooling, on shaping the broadband synchrotron spectra of PWNe. We also consider the turbulent reconnection of magnetic fields in PWs to account for the source of turbulence, as well as the injection of energetic particles for further ASA and synchrotron radiation in PWNe.

Based on the modern understanding of MHD turbulence and its interaction with energetic particles mentioned above, we apply our analytical model for describing the ASA and radiation loss to PWNe and aim at providing a general explanation for their broken power-law spectra. The structure of this paper is as follows. In Section 2, we present our analytical model and elucidate the physical origin of the broken power-law spectrum in the context of a PWN. In Section 3, we take the Mouse PWN and some other PWNe as examples for

[4] Hubble Fellow.

applying our theoretical model to the observed broadband synchrotron spectra. Lastly, a discussion and a summary are given in Sections 4 and 5, respectively.

2. Physical Origin of a Broken Power-law Spectrum of a PWN

2.1. Turbulent Reconnection in the PW

To facilitate the transition from the Poynting-flux-dominated (i.e., high-σ) PW (Arons 2002) to the particle energy flux-dominated (i.e., low-σ) downstream of the termination shock (Rees & Gunn 1974; Kennel & Coroniti 1984; Begelman & Li 1992; Bogovalov et al. 2005), efficient dissipative processes are necessary to convert the magnetic energy to kinetic energy in the upstream wind or at the termination shock. Magnetic reconnection serves as the required dissipation mechanism (Del Zanna et al. 2016). It can occur in the striped wind with alternating magnetic fields (Coroniti 1990; Lyubarsky & Kirk 2001), as well as the kink-unstable polar jet (Begelman 1998; Pavlov et al. 2003; Mizuno et al. 2011; Mignone et al. 2013).

In resistive MHD theory, the magnetic reconnection depends on the slow resistive diffusion of magnetic fields (Sweet 1958; Parker 1957). In the presence of turbulence, turbulent velocities dominate the magnetic field dynamics in the direction perpendicular to the local magnetic field (LV99). The turbulent velocities act to increase the magnetic field gradients along the turbulent energy cascade toward smaller scales, and thus enhance the reconnection and determine the actual reconnection efficiency. In strongly magnetized turbulence, the reconnection rate is given by (LV99)

$$v_{\rm rec} \approx V_{\rm A}\sqrt{\frac{L_i}{L_x}}M_{\rm A}^2, \quad (1)$$

when the injection scale of turbulence L_i is smaller than the length of the current sheet L_x, and

$$v_{\rm rec} \approx V_{\rm A}\sqrt{\frac{L_x}{L_i}}M_{\rm A}^2 \quad (2)$$

when $L_i > L_x$. Here $v_{\rm rec}$ is the reconnection speed, $V_{\rm A}$ is the Alfvén speed, and $M_{\rm A}$ is the ratio of the turbulent speed at L_i to $V_{\rm A}$. Without the constraint imposed by the microscopic diffusion process, turbulent reconnection can be highly efficient with $v_{\rm rec}$ up to $V_{\rm A}$. Numerical experiments in both nonrelativistic (Kowal et al. 2009) and relativistic (East et al. 2015; Takamoto et al. 2015; Zrake & East 2016) plasmas confirm that the turbulent reconnection is universal with respect to microscopic physics, e.g., resistive diffusion.

Magnetic reconnection itself acts as a source of turbulence. The magnetostatic free energy carried by the striped wind can be readily converted to turbulent energy via magnetic reconnection (East et al. 2015; Zrake & East 2016). The generated turbulence in turn boosts the reconnection efficiency as discussed above (Kowal et al. 2017). This positive feedback can result in a runaway reconnection and explosive release of magnetic energy, accounting for the energy source of observed γ-ray flares from, e.g., the Crab Nebula (Abdo et al. 2011; Tavani et al. 2011). The development of both turbulence and turbulent reconnection of magnetic fields have been observed in numerical simulations of the pulsar striped wind, e.g., Zrake (2016).

Moreover, magnetic reconnection can also efficiently energize particles (de Gouveia dal Pino & Lazarian 2005; Kowal et al. 2011, 2012; del Valle et al. 2016), which supplies the PWN with a power-law population of energetic electrons. By adopting a simple treatment analogous to that for the first-order Fermi acceleration at shocks, de Gouveia dal Pino & Lazarian (2005) derived a power-law index of 2.5 for the reconnection-accelerated particles. Beyond the termination shock, the spectrum of the accelerated electrons injected into the PWN will be affected by both the ASA and synchrotron cooling in the turbulent magnetic fields downstream.

2.2. ASA in the PWN

Due to the magnetic reconnection in the striped wind, the PWN is expected to be fully turbulent. The Kolmogorov-like magnetic energy spectrum has been found in 3D relativistic MHD simulations of PWNe, e.g., Porth et al. (2014b), which is a typical spectral form of turbulent magnetic fields in strong MHD turbulence (Maron & Goldreich 2001; Cho & Lazarian 2003).

In strong MHD turbulence with increased turbulence anisotropy toward smaller scales, the turbulent eddies at the resonant scale of gyroresonance are highly elongated along the magnetic field. With the perpendicular scale of the turbulent eddies much smaller than the parallel resonant scale, particles interact with many uncorrelated turbulent eddies within one gyro orbit, and thus the gyroresonance scattering is inefficient (Chandran 2000; Yan & Lazarian 2002). In the absence of efficient scattering, relativistic particles can slide along magnetic field lines. Obviously, the magnetic field variation is slow with respect to the motion of particles. Within the traps of turbulent eddies, the second (longitudinal) adiabatic invariant of the particles bouncing between the "mirror points" applies. As there are statistically distributed reconnection and dynamo regions in strong MHD turbulence (Xu & Lazarian 2016), after cycles of acceleration in turbulent reconnection regions with shrinking field lines and cycles of deceleration in turbulent dynamo regions with stretched field lines, the particles have a diffusive energy gain (Brunetti & Lazarian 2016). We term this acceleration process as the "ASA" (Xu & Zhang 2017; Xu et al. 2018).

The acceleration rate of the ASA is

$$a_{\rm A} = \xi\frac{u_{\rm tur}}{l_{\rm tur}}, \quad (3)$$

where $l_{\rm tur}$ is the characteristic scale of turbulent magnetic fields, $u_{\rm tur}$ is the turbulent speed at $l_{\rm tur}$, and their ratio gives the corresponding turbulent eddy-turnover time $\tau_{\rm tur}$. ξ represents the cumulative fractional energy change during $\tau_{\rm tur}$. As relativistic particles undergo the first-order Fermi process within individual eddies, given the number of bounces $\sim c/u_{\rm tur}$ and the energy change per bounce $\sim u_{\rm tur}/c$, where c is the speed of light, we can easily see that ξ is of order unity. Thus the ASA is a very efficient stochastic acceleration mechanism compared to the second-order Fermi acceleration associated with gyroresonance scattering.

2.3. Synchrotron Spectrum under the Effects of ASA and Synchrotron Cooling

The stochastic acceleration generally leads to energy diffusion and a hard energy spectrum of particles. We consider

a steady injection of a power-law distribution of electrons originating from the magnetic reconnection sites in the PW (Section 2.1),

$$Q(E) = CE^{-p}, \quad E_l < E < E_u. \tag{4}$$

At a given reference energy, C is the electron number per unit energy per unit time, p is the power-law index, and E_l and E_u are the lower and upper energy limits, respectively. Due to the ASA, the energy distribution of electrons spreads out in energy space following (Melrose 1969)

$$E \sim \exp(\pm 2\sqrt{a_{\rm A} t}). \tag{5}$$

The injected energy spectrum evolves with time t and approaches a universal form (Xu et al. 2018)

$$N(E, t) = \frac{C(E_u^{-p+1} - E_l^{-p+1})\sqrt{t}}{(-p+1)\sqrt{\pi a_{\rm A}}} E^{-1} \exp\left(-\frac{E}{E_{\rm cf}}\right), \quad E_m < E < E_{\rm cf}. \tag{6}$$

The resulting energy spectrum has a minimum energy E_m. It is smaller than E_l as the energy spectrum under the effect of ASA tends to have a larger energy spread than that of the injected electrons (Equation (5)). $E_{\rm cf}$ is the cutoff energy of the ASA and has the expression

$$E_{\rm cf} = \frac{a_{\rm A}}{\beta}, \tag{7}$$

corresponding to the equalization between $a_{\rm A}$ and synchrotron cooling rate. Here the parameter β is given by

$$\beta = \frac{P_{\rm syn}}{E^2} = \frac{\sigma_{\rm T} c B^2}{6\pi (m_e c^2)^2}, \tag{8}$$

where $P_{\rm syn}$ is the power of synchrotron radiation, B is the magnetic field strength, $\sigma_{\rm T}$ is the Thomson cross section, and m_e is the electron rest mass. Different from a steep energy spectrum of electrons, for which the minimum energy is the characteristic electron energy, for a hard electron spectrum in Equation (6), the upper cutoff energy $E_{\rm cf}$ dominates the integral,

$$\int_{E_m}^{E_{\rm cf}} EN(E)dE \approx \frac{C(E_u^{-p+1} - E_l^{-p+1})\sqrt{t}}{(-p+1)\sqrt{\pi a_{\rm A}}} E_{\rm cf} = \epsilon \dot{E} t, \tag{9}$$

where we assume $E_u < E_{\rm cf}$ and $E_m \ll E_{\rm cf}$, $\dot{E}$ is the spin-down power of the pulsar, and ϵ is the fraction of the spin-down energy converted to the particle energy. To confront the above relation to observations, a detailed modeling of the particle acceleration in the PW is needed, which is beyond the scope of the current paper.

We next consider that the injected electrons have sufficiently high energies with $E_{\rm cf} < E_u$. The hard electron energy distribution below $E_{\rm cf}$ is attributed to the ASA, while the distribution at energies above $E_{\rm cf}$ is governed by synchrotron cooling effect. By defining the critical cooling energy (Sari et al. 1998)

$$E_c = P_{\rm syn} t = \frac{1}{\beta t}, \tag{10}$$

we see that the injected electrons with $E > E_c > E_{\rm cf}$ cool down to E_c within time t. But the electrons with $E < E_{\rm cf}$ do not cool because of the ASA, irrespective of the value of E_c. It means that the overall system is always in the slow cooling regime.

Given E_m and E_u as the lower and upper energy limits of the entire electron energy spectrum, depending on the relation between E_l, $E_{\rm cf}$, and E_c, the electron spectrum at $E > E_{\rm cf}$ can exhibit different forms (Xu et al. 2018).

Case (i): $E_c < E_l < E_{\rm cf}$

In the energy range above $E_{\rm cf}$, the cooled electrons follow a steep spectrum (Kardashev 1962)

$$N(E) = \frac{CE^{-(p+1)}}{\beta(p-1)}. \tag{11}$$

Combining Equations (6) and (11), we illustrate the asymptotic behavior of the electron spectrum over a broad energy range in Figure 1(a). The corresponding synchrotron spectrum is

$$\nu F_\nu = \nu F_{\nu,\max} \propto \nu, \quad \nu < \nu_{\rm cf}, \tag{12a}$$

$$\nu F_\nu = \nu F_{\nu,\max} \left(\frac{\nu}{\nu_{\rm cf}}\right)^{-\frac{p}{2}} \propto \nu^{-\frac{p}{2}+1}, \quad \nu > \nu_{\rm cf}, \tag{12b}$$

as displayed in Figure 1(b), where $\nu_{\rm cf}$ is the frequency related to $E_{\rm cf}$, F_ν is the flux density at frequency ν, and $F_{\nu,\max}$ is the maximum value of F_ν.

Case (ii): $E_c < E_{\rm cf} < E_l$

In the energy range above E_l, the same steep electron spectrum as in Equation (11) applies. Moreover, driven by the cooling effect, the injected electron energy distribution extends down to lower energies. In the energy range $E_{\rm cf} < E < E_l$, the electron spectrum is $N(E) \sim E^{-2}$, with the injection and radiation losses of electrons in equilibrium (Melrose 1969). Accordingly, the entire electron spectrum contains three segments, as shown in Figure 1(c). The corresponding synchrotron spectrum is (see Figure 1(d)),

$$\nu F_\nu = \nu F_{\nu,\max} \propto \nu, \quad \nu < \nu_{\rm cf}, \tag{13a}$$

$$\nu F_\nu = \nu F_{\nu,\max} \left(\frac{\nu}{\nu_{\rm cf}}\right)^{-\frac{1}{2}} \propto \nu^{\frac{1}{2}}, \quad \nu_{\rm cf} < \nu < \nu_l, \tag{13b}$$

$$\nu F_\nu = \nu F_{\nu,\max} \left(\frac{\nu_l}{\nu_{\rm cf}}\right)^{-\frac{1}{2}} \left(\frac{\nu}{\nu_l}\right)^{-\frac{p}{2}} \propto \nu^{-\frac{p}{2}+1}, \quad \nu > \nu_l, \tag{13c}$$

where ν_l is related to E_l.

Case (iii): $E_l < E_c < E_{\rm cf}$

As shown in Figure 2(a), $N(E)$ in this situation has the same form as that in *Case (i)*. The resulting synchrotron spectrum also has the same shape as that in Equation (12), which can be seen in Figure 2(b).

Case (iv): $E_l < E_{\rm cf} < E_c$

The cooled electrons at $E > E_c$ still follow the spectral shape as in Equation (11), while the electrons in the energy range $E_{\rm cf} < E < E_c$ are not subjected to the cooling effect, so their original spectral form remains (see Figure 2(c)). Then the synchrotron spectrum is given by (Figure 1(d)),

$$\nu F_\nu = \nu F_{\nu,\max} \propto \nu, \quad \nu < \nu_{\rm cf}, \tag{14a}$$

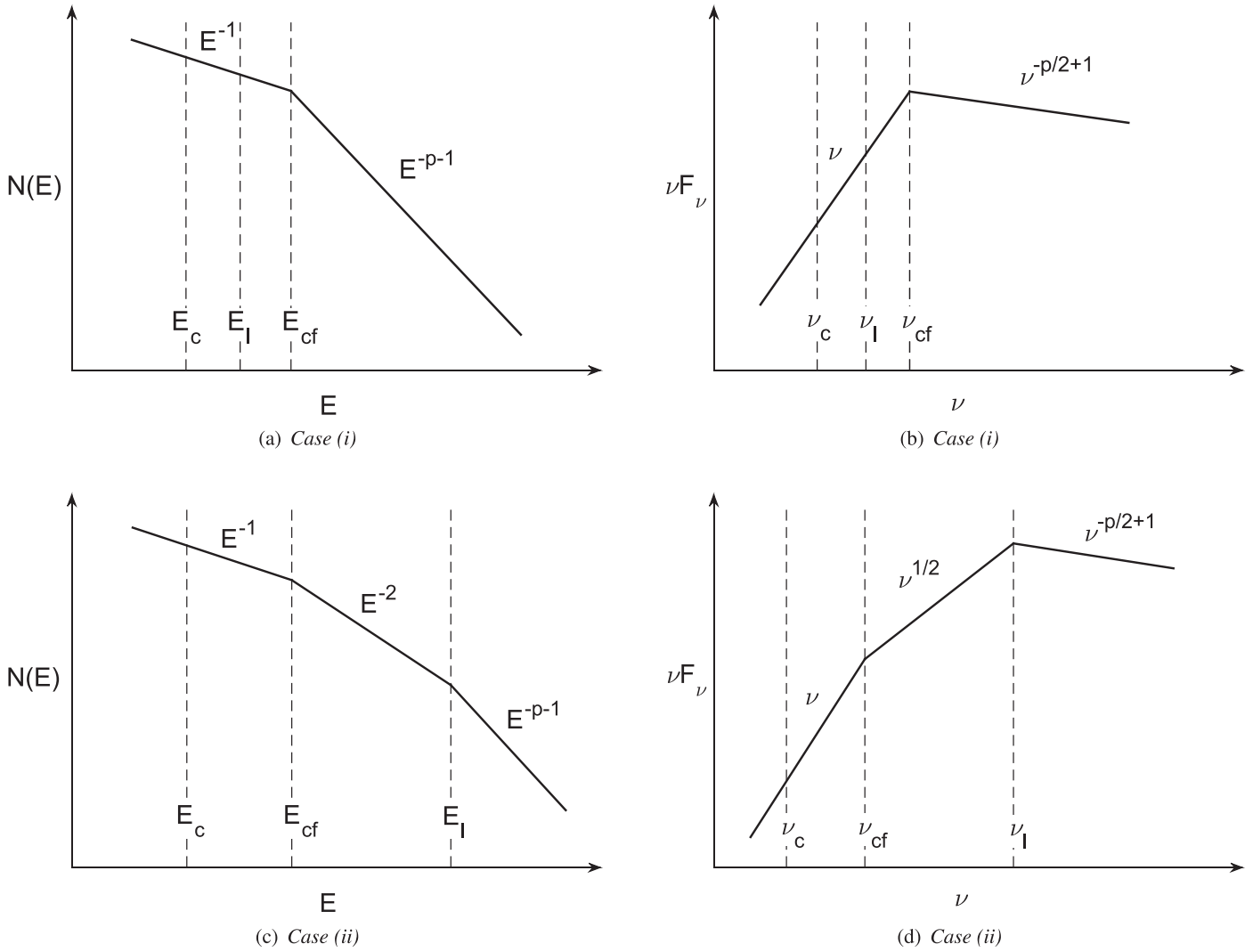

(a) *Case (i)* (b) *Case (i)*

(c) *Case (ii)* (d) *Case (ii)*

Figure 1. Electron energy spectrum ((a) and (c)) under the effects of ASA and synchrotron cooling and the corresponding synchrotron spectrum ((b) and (d)) in *Case (i)* and *Case (ii)*.

$$\nu F_\nu = \nu F_{\nu,\max}\left(\frac{\nu}{\nu_{\rm cf}}\right)^{-\frac{p-1}{2}} \propto \nu^{-\frac{p-3}{2}}, \quad \nu_{\rm cf} < \nu < \nu_c, \tag{14b}$$

$$\nu F_\nu = \nu F_{\nu,\max}\left(\frac{\nu_c}{\nu_{\rm cf}}\right)^{-\frac{p-1}{2}}\left(\frac{\nu}{\nu_c}\right)^{-\frac{p}{2}} \propto \nu^{-\frac{p}{2}+1}, \quad \nu > \nu_c, \tag{14c}$$

where ν_c corresponds to E_c. It has a similar form to that in *Case (ii)* (Equation (13)) except for the intermediate segment.

In all the above cases, we also expect $\nu F_\nu \propto \nu^{4/3}$ at $\nu < \nu_m$ (not shown in Figures 1 and 2), where ν_m corresponds to E_m. This low-frequency power-law index is a characteristic feature of synchrotron radiation and is independent of the detailed electron energy spectrum (Rybicki & Lightman 1979; Meszaros & Rees 1993).

The above analysis shows that the dominance of the ASA at low energies and synchrotron cooling at high energies naturally gives rise to broken power-law electron and synchrotron spectra. Moreover, depending on the relation between E_l, $E_{\rm cf}$, and E_c, the spectrum can have various forms at intermediate energies (frequencies).

3. Comparisons between Analytical Spectral Shapes and Observed Spectra of PWNe

The synchrotron emission of PWNe is characterized by a broadband spectrum. It typically has a flat radio component with $F_\nu \propto \nu^\alpha$, where $-0.3 \lesssim \alpha \lesssim 0$, and a steep X-ray component with $\alpha \sim -1$ (Chevalier 2005; Gaensler & Slane 2006; Reynolds et al. 2017). We apply the above theoretical model to interpret the spectral shape of the Mouse PWN (Section 3.1) and some other PWNe with well-characterized multiwavelength spectra (Section 3.2). Here we aim at explaining the overall spectral shapes, rather than providing detailed fits for individual sources.

3.1. Application to the Mouse PWN

Figure 3(a) presents the observed multiwavelength spectrum of G359.23-0.82, a.k.a., the Mouse PWN powered by PSR J1747-2958. Over the radio and X-ray data points taken from Klingler et al. (2018; hereafter K18), we first assume the spectral shape given in Equation (12) corresponding to *Case (i)*

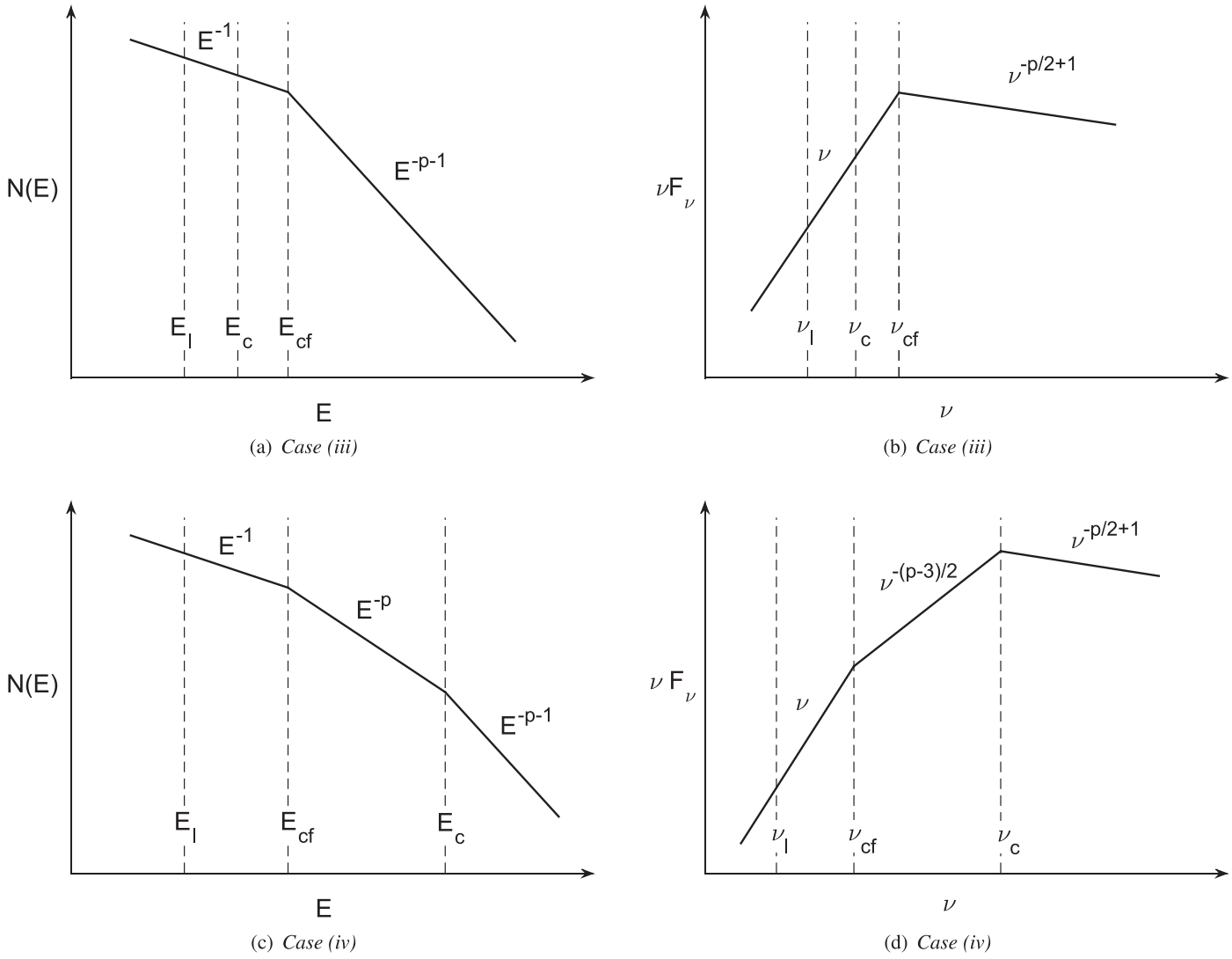

(a) *Case (iii)* (b) *Case (iii)*

(c) *Case (iv)* (d) *Case (iv)*

Figure 2. The same as Figure 1 but for *Case (iii)* and *Case (iv)*.

or *Case (iii)* in Section 2.3. Here we adopt $p = 2.18$ according to the fit to the X-ray data in K18. We see that the two spectral segments dominated by the ASA and radiation losses separately match the radio and X-ray data.

The photon energy $E_{\rm ph}$ is related to the electron Lorentz factor γ_e by

$$E_{\rm ph} = \hbar \frac{eB}{m_e c} \gamma_e^2 \Gamma, \tag{15}$$

with $\hbar = h/2\pi$, the Planck constant h, the electron charge e, the Lorentz factor $\Gamma(\approx 1)$ of the mildly relativistic bulk flow in the PWN (Reynolds et al. 2017). The lowest observed photon energy $E_{\rm ph,m} = 6.2 \times 10^{-7}$ eV provides the upper limit of $\gamma_{e,\rm m} = E_m/(m_e c^2)$,

$$\gamma_{e,\rm m,max} = 5.2 \times 10^2 \left(\frac{\Gamma}{1}\right)^{-\frac{1}{2}} \left(\frac{B}{200\ \mu\rm G}\right)^{-\frac{1}{2}} \left(\frac{E_{\rm ph,m}}{6.2 \times 10^{-7}\ \rm eV}\right)^{\frac{1}{2}}. \tag{16}$$

Here we adopt the equipartition magnetic field $B \sim 200\ \mu$G estimated in K18.

The spectral break appears at the photon energy $E_{\rm ph,b} \approx 9 \times 10^{-3}$ eV. It is related to the cutoff electron energy $E_{\rm cf} = \gamma_{e,\rm cf} m_e c^2$ and signifies the balance between acceleration and cooling. So we have

$$\gamma_{e,\rm cf} = 6.2 \times 10^4 \left(\frac{\Gamma}{1}\right)^{-\frac{1}{2}} \left(\frac{B}{200\ \mu\rm G}\right)^{-\frac{1}{2}} \left(\frac{E_{\rm ph,b}}{9 \times 10^{-3}\ \rm eV}\right)^{\frac{1}{2}}. \tag{17}$$

It gives the upper limit of the minimum Lorentz factor of injected electrons $\gamma_{e,l} = E_l/(m_e c^2)$ in this scenario. It also gives the minimum cooling time for the condition $E_c < E_{\rm cf}$ to be satisfied (Equations (8), (10), and (17)),

$$t_{\rm c,min} = \frac{1}{E_{\rm cf}\beta} = \frac{1}{\gamma_{e,\rm cf} m_e c^2 \beta} = 9.9 \left(\frac{\Gamma}{1}\right)^{\frac{1}{2}} \left(\frac{B}{200\ \mu\rm G}\right)^{-\frac{3}{2}} \left(\frac{E_{\rm ph,b}}{9 \times 10^{-3}\ \rm eV}\right)^{-\frac{1}{2}} \rm kyr. \tag{18}$$

Besides, the maximum cooling time $t_{\rm c,max}$ is given by the spin-down age $t_{\rm sd} = 25.5$ kyr of the pulsar (K18). It corresponds to

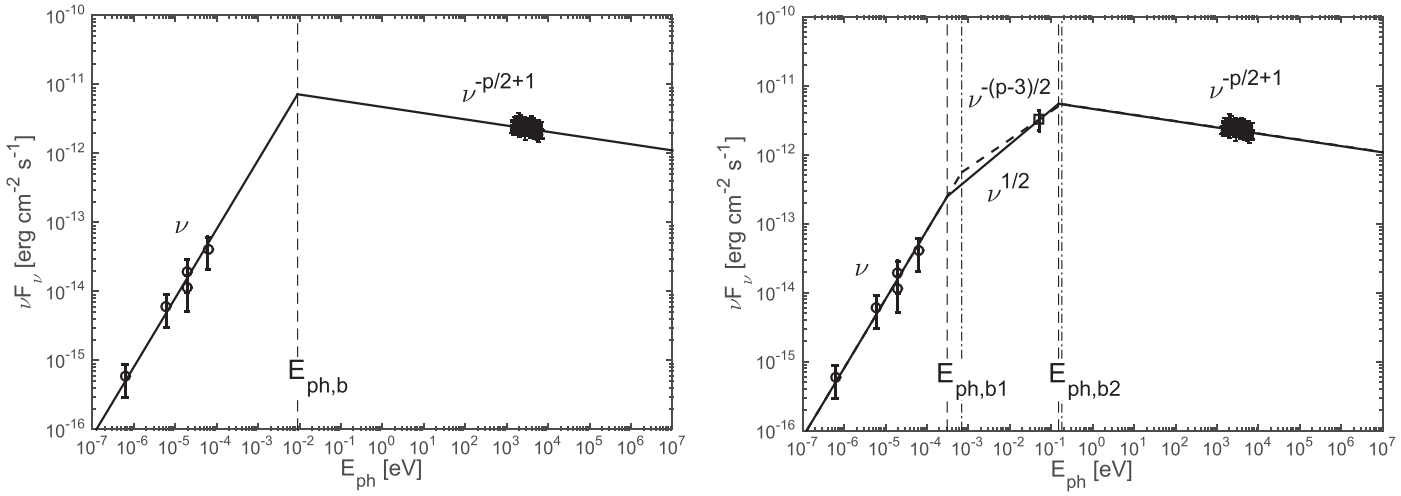

Figure 3. Our analytical spectral shapes in comparison with the data points of the Mouse PWN taken from K18. Circles, squares, and dots represent radio, infrared, and X-ray data, respectively. The spectral shapes are given by Equation (12) (solid line) in (a), and Equation (13) (solid line) and Equation (14) (dashed line) in (b). The vertical lines indicate break energies.

Table 1
Characteristic Parameters Inferred from the Spectral Breaks of the Mouse PWN

$E_{\rm ph}$	$E_{\rm ph,m}$	$E_{\rm ph,b}$ or $E_{\rm ph,b1}$	$E_{\rm ph,b2}$
Case (i) or *Case (iii)*	$\gamma_{e,\rm m} \approx 5.2 \times 10^2$	$\gamma_{e,\rm cf} = \gamma_{e,l,\rm max} \approx 6.2 \times 10^4$, $\tau_{\rm acc} = t_{\rm c,min} \approx 9.9$ kyr	⋯
Case (ii)		$\gamma_{e,\rm cf} \approx 1.1 \times 10^4$, $\tau_{\rm acc} = t_{\rm c,min} \approx 53.5$ kyr	$\gamma_{e,l} \approx 2.5 \times 10^5$
Case (iv)		$\gamma_{e,\rm cf} = \gamma_{e,l,\rm max} \approx 1.7 \times 10^4$,$\tau_{\rm acc} \approx 35.8$ kyr	$t_c \approx 2.2$ kyr

the electron Lorentz factor (Equations (8), (10), and (16)),

$$\gamma_{e,\rm sd} = \frac{1}{m_e c^2 \beta t_{\rm sd}} = 2.4 \times 10^4 \left(\frac{B}{200\ \mu\rm G}\right)^{-2} \left(\frac{t_{\rm sd}}{25.5\ \rm kyr}\right)^{-1} > \gamma_{e,\rm m,max}, \quad (19)$$

implying that the electrons in the Mouse PWN are in the slow cooling regime with $E_{c,\rm min} > E_{m,\rm max}$ (see also K18 for the analysis of the cooling regime).

Moreover, $t_{\rm c,min}$ in Equation (18) also gives the acceleration timescale of the ASA (Equation (7)),

$$\tau_{\rm acc} = a_{\rm A}^{-1} = t_{\rm c,min}. \quad (20)$$

We note that $\tau_{\rm acc}$ in *Case (i)* or *Case (iii)* is shorter than t_c.

Including the tentative infrared point (see Figure 3(b) and K18)[5] requires the spectral shape given by Equation (13) in *Case (ii)* or Equation (14) in *Case (iv)*. The spectral breaks at lower and higher energies are $E_{\rm ph,b1} \approx 3.1 \times 10^{-4}$ eV, $E_{\rm ph,b2} \approx 0.15$ eV in *Case (ii)*, and $E_{\rm ph,b1} \approx 6.9 \times 10^{-4}$ eV, $E_{\rm ph,b2} \approx 0.18$ eV in *Case (iv)*. Similar to the above analysis, these break energies can be used to infer the characteristic γ_e, t_c, and $\tau_{\rm acc}$ (Equations (15), (18), and (20)), as shown in Table 1. We see that because the minimum t_c required in *Case (ii)* is much larger than $t_{\rm sd}$ of the pulsar, *Case (ii)* is disfavored.

The above comparisons show that our analytical spectral shapes agree well with the observed multiwavelength spectrum of the Mouse PWN. The ASA and synchrotron cooling in the PWN naturally account for the flatness and steepness of the radio and X-ray spectra (F_ν), respectively. More reliable infrared measurements with, e.g., *Hubble Space Telescope* (*HST*), *James Webb Space Telescope*, and *ALMA* are needed to determine the detailed spectral shape at intermediate energies and to distinguish between *Case (i)* (or *Case (iii)*) and *Case (iv)*.

3.2. Application to Some Other PWNe

We next compare our analytical spectral shapes with the synchrotron spectra of some other PWNe to further examine the applicability of our model.

In Figure 4, we display the synchrotron spectra of 3C 58 (Slane et al. 2008), G21.5–0.9 (Salter et al. 1989), G0.9 + 0.1 (Tanaka & Takahara 2011), and N157B (Zhu et al. 2018). We also include the infrared data for 3C 58, but we caution that the observed values are only upper limits (Slane et al. 2008). The X-ray data for G21.5–0.9 and N157B were obtained from *Chandra* ObsIDs 2873, 3699 3700, 5158, 5159, 5165, 5166, 6070, 6071, 6740, 6741, 8371, 8372 (G21.5–0.9), and 2783 (N157B). The data were reprocessed using the *Chandra* Interactive Analysis of Observations software version 4.9 and the *Chandra* Calibration Data Base version 4.7.7. All observations were reprocessed with `chandra_repro` to apply the latest calibrations. We extracted the spectra using `specextract` and fitted the power-law spectra using the `tbabs` model of XSPEC (v12.9.1p, which uses absorption cross-sections from Wilms et al. 2000). For G21.5–0.9 we use a circular 2.′5 aperture centered on the pulsar, and excluding the bright point source to the south. For N157B, we use a

[5] We caution that the connection of this infrared emission to the Mouse PWN needs further examination by high-resolution infrared observations (K18).

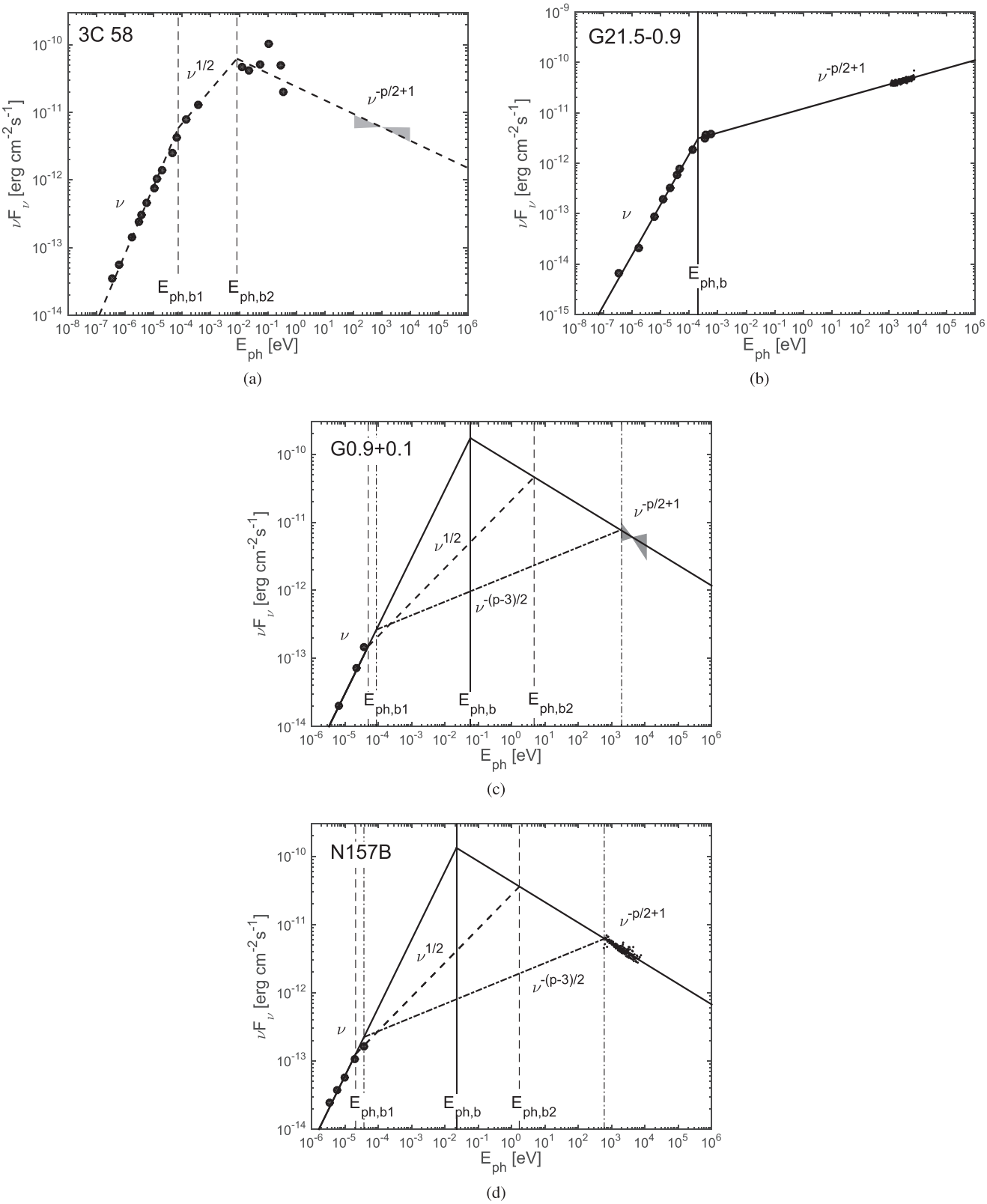

Figure 4. Our analytical spectral shapes (solid line: Equation (12), dashed line: Equation (13), dashed–dotted line: Equation (14)) in comparison with the observed synchrotron spectra of PWNe. Vertical lines indicate break energies.

$53'' \times 24''$ extraction region approximately coincident with the brightest radio contour shown in Figure 3 of Chen et al. (2006) and free of thermal supernova remnant (SNR) filaments. In both cases we use background regions located outside the extent of the PWNe/SNRs, and restricted the spectral fits to the 0.5–8 keV range. We verified that our results are not noticeably contaminated by thermal SNR emission by restricting the spectral fits to energies above 2 keV and refitting; in both cases

Table 2
Parameters of the PWNe

PWNe	Mouse	3C 58	G21.5–0.9	G0.9+0.1	N157B
$E_{\rm ph,b}$ [eV]	9.0×10^{-3}	...	2.1×10^{-4}	5.8×10^{-2}	2.2×10^{-2}
$E_{\rm ph,b1,min}$ [eV]	3.1×10^{-4}	7.3×10^{-5}	...	5.0×10^{-5}	2.1×10^{-5}
$B_{\rm eq}$ [μG]	200[a]	60[b]	180[c]	56[d]	230[e]

Notes.
[a] K18.
[b] Reynolds & Aller (1988).
[c] Safi-Harb et al. (2001).
[d] Dubner et al. (2008).
[e] Wang et al. (2001).

the resulting power-law slopes were virtually identical. Our fits to the X-ray data imply $p = 1.68$ for G21.5–0.9 and $p = 2.6$ for N157B. For 3C 58 and G0.9+0.1, we use $p = 2.4$ and $p = 2.6$ according to the fits to their X-ray data (Slane et al. 2008; Tanaka & Takahara 2011).

For 3C 58 and G21.5–0.9, as indicated by the data, we apply the spectral shape in Equation (13) (*Case (ii)*) and that in Equation (12) (*Case (i)* or *Case (iii)*), respectively. For G0.9+0.1 and N157B, the measurements are insufficient to constrain the detailed spectral form in the intermediate energy range, so we present all possible spectral shapes for comparison with future observations. In all cases, it is clear that the electrons in the PWN should undergo the stochastic acceleration to account for the radio spectrum. The general agreement between our analytical spectral shapes and observed spectra implies the ASA and synchrotron cooling together as a common origin of broadband synchrotron spectra of PWNe.

The spectral break between radio and X-ray bands or radio and infrared bands is determined by $\tau_{\rm acc}$ of the ASA. When $\tau_{\rm acc}$ is sufficiently short for $E_{\rm cf}$ to be larger than both E_c and E_l, the synchrotron spectrum of a PWN falls in *Case (i)* or *Case (iii)*. Then we can rewrite Equation (18) as

$$\left(\frac{\tau_{\rm acc}}{1\ {\rm kyr}}\right)\left(\frac{B}{100\ \mu{\rm G}}\right)^{\frac{3}{2}} = 26.5\left(\frac{\Gamma}{1}\right)^{\frac{1}{2}}\left(\frac{E_{\rm ph,b}}{10^{-2}\ {\rm eV}}\right)^{-\frac{1}{2}}, \quad (21)$$

and obtain a constraint on $\tau_{\rm acc}$ and B in the PWN. When $\tau_{\rm acc}$ is relatively long with $E_{\rm cf} < E_l$ or $E_{\rm cf} < E_c$, the PWN is in *Case (ii)* or *Case (iv)*. Accordingly, we have

$$\left(\frac{\tau_{\rm acc}}{1\ {\rm kyr}}\right)\left(\frac{B}{100\ \mu{\rm G}}\right)^{\frac{3}{2}} = 837.0\left(\frac{\Gamma}{1}\right)^{\frac{1}{2}}\left(\frac{E_{\rm ph,b1}}{10^{-5}\ {\rm eV}}\right)^{-\frac{1}{2}}. \quad (22)$$

If the spectral shape in the infrared band cannot be observationally determined (e.g., G0.9+0.1, N157B), we can still set a constraint on the range of $\tau_{\rm acc}$ and B,

$$26.5\left(\frac{\Gamma}{1}\right)^{\frac{1}{2}}\left(\frac{E_{\rm ph,b}}{10^{-2}\ {\rm eV}}\right)^{-\frac{1}{2}} \leqslant \left(\frac{\tau_{\rm acc}}{1\ {\rm kyr}}\right)\left(\frac{B}{100\ \mu{\rm G}}\right)^{\frac{3}{2}} \leqslant 837.0\left(\frac{\Gamma}{1}\right)^{\frac{1}{2}}\left(\frac{E_{\rm ph,b1}}{10^{-5}\ {\rm eV}}\right)^{-\frac{1}{2}}. \quad (23)$$

In Table 2, we list the values of $E_{\rm ph,b}$ and $E_{\rm ph,b1}$ of the above PWNe. For G0.9+0.1 and N157B, we can only provide the lower limit of $E_{\rm ph,b1}$ due to the insufficient data points. By using the estimated magnetic field strength $B_{\rm eq}$ under the assumption of equipartition between particle and magnetic energies (see Table 2), in Figure 5 we present the corresponding $\tau_{\rm acc}$ (Equations (21) and (22)) or the range of $\tau_{\rm acc}$ (Equation (23)) inferred from the spectral breaks of the PWNe. Empirically, we see that $\tau_{\rm acc}$ of different PWNe are basically within the range confined by Equation (23).

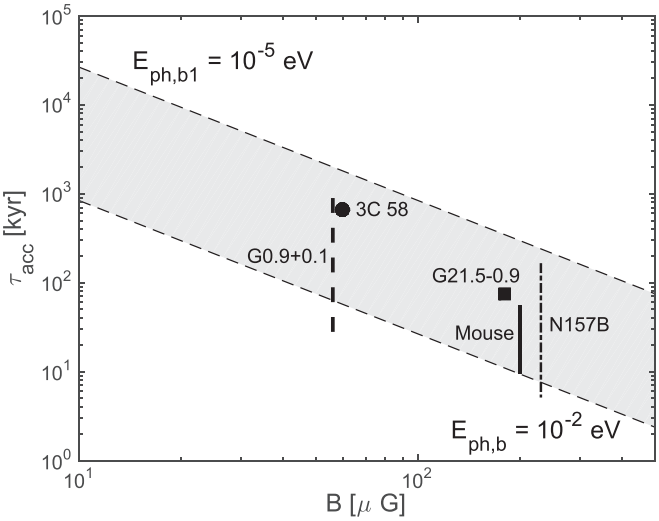

Figure 5. $\tau_{\rm acc}$ vs. $B_{\rm eq}$ of the PWNe. The shaded region is bounded by Equation (23).

4. Discussion

Turbulence is believed to be present in PWNe, but its origin and properties are unclear. Besides the magnetic reconnection under consideration here, other possible sources of turbulence include, e.g., the Rayleigh–Taylor instability induced by the interaction between the PWN and the SNR (Chevalier & Gull 1975; Porth et al. 2014a), the dynamical instability of the PW's oscillating magnetic field (Zrake 2016), the Weibel instability (Weibel 1959; Sironi & Spitkovsky 2011), the large-scale shear flows in the PWN (Komissarov & Lyubarsky 2004). For bow-shock PWNe, an additional source of turbulence can be the Richtmyer–Meshkov instability induced by their interaction with interstellar density fluctuations (Giacalone & Jokipii 2007). As a more general mechanism to generate turbulence, the magnetic reconnection is dynamically coupled with turbulence and naturally converts magnetic energy to turbulent energy. The generated turbulence allows efficient dissipation of magnetic energy through turbulent reconnection in the PW, and further ASA of the electrons in the PWN.

Non-ASA including the gyroresonance and transit time damping (TTD) can also result in a hard electron spectrum (Melrose 1969). As is known, the gyroresonance with Alfvén modes is inefficient due to the turbulence anisotropy (Chandran 2000; Yan & Lazarian 2002), while TTD with compressive fast and slow modes can be alternative stochastic acceleration mechanisms (Yan & Lazarian 2008; Xu & Lazarian 2018). However, only a small fraction of turbulent energy is contained in compressive modes in compressible MHD turbulence (Cho & Lazarian 2002; Kowal & Lazarian 2010). Moreover, fast modes are usually subjected to severe plasma damping effects (Yan & Lazarian 2004), and TTD with slow modes also suffers the turbulence anisotropy (Xu & Lazarian 2018). We note that the turbulence anisotropy is scale-dependent (Cho & Lazarian 2003). Even at a low magnetization in outer regions of PWNe, the turbulent eddies at the small resonant scale are still highly anisotropic. Therefore, when the pitch-angle scattering and non-ASA are inefficient, the ASA can account for the stochastic acceleration in PWNe. Since the largest eddies are most effective in ASA, its efficiency does not depend on the turbulence spectral slope. We find numerical evidence for the ASA in both MHD simulations (Lynn et al. 2012) and kinetic particle-in-cell simulations (Dahlin et al. 2017). Obviously, in a situation where the pitch-angle scattering is efficient and thus the adiabatic invariance is violated, the ASA is suppressed.

The ASA occurs when the Larmor radius r_L of electrons is much smaller than the characteristic length scale of turbulent magnetic fields. The largest r_L of the stochastically accelerated electrons corresponding to $E_{\rm ph,b}$ is (Equation (17))

$$r_L = \frac{\gamma_{e,\rm cf} m_e c^2}{eB} = 1.6\times 10^{12}\left(\frac{\Gamma}{1}\right)^{-\frac{1}{2}}\left(\frac{B}{100\ \mu\rm G}\right)^{-\frac{3}{2}}\left(\frac{E_{\rm ph,b}}{10^{-2}\ \rm eV}\right)^{\frac{1}{2}}\ \rm cm. \quad (24)$$

It is indeed small compared with the characteristic turbulence scale of the order of 0.1 pc suggested by polarization observations of PWNe (e.g., Yusef-Zadeh & Gaensler 2005; Moran et al. 2013; Ma et al. 2016). Given the turbulence scale $l_{\rm tur}$ and $\tau_{\rm acc}$, we can also estimate the turbulent speed at $l_{\rm tur}$ (Equations (3), (18), and (20))

$$u_{\rm tur} = \xi^{-1} l_{\rm tur}\tau_{\rm acc}^{-1} = 3.7\left(\frac{\xi}{1}\right)^{-1}\left(\frac{\Gamma}{1}\right)^{-\frac{1}{2}}\left(\frac{B}{100\ \mu\rm G}\right)^{\frac{3}{2}}\left(\frac{E_{\rm ph,b}}{10^{-2}\ \rm eV}\right)^{\frac{1}{2}} \times\left(\frac{l_{\rm tur}}{0.1\ \rm pc}\right)\rm km\ s^{-1}. \quad (25)$$

If we assume that the interstellar turbulence driven by supernova explosions has $L_i \sim 100$ pc and the turbulent speed $V_L \sim 10\ \rm km\ s^{-1}$ at L_i (Kaplan & Pikelner 1970), then according to the Kolmogorov scaling (Armstrong et al. 1995; Chepurnov & Lazarian 2010), the turbulent speed in the interstellar medium at 0.1 pc is $v_l = V_L(l/L_i)^{1/3} \sim 1\ \rm km\ s^{-1}$. It implies that the turbulence level in a PWN can be comparable to the surrounding interstellar turbulence.

We have analyzed the synchrotron spectra of both bow-shock PWN (Mouse) and PWNe SNRs (3C 58, G21.5–0.9, G0.9+0.1, N157B). Despite their possibly different interaction with ambient media, all PWNe exhibit broken power-law spectra with a flat radio component (F_ν) and a steeper X-ray component. This common feature implies that both stochastic acceleration and synchrotron cooling of electrons generally exist in different types of PWNe. Relativistic MHD simulations of PWNe also support that radio emitting particles undergo a local reacceleration process in the nebula by the interaction with turbulence (Olmi et al. 2014, 2016).

The ASA is a promising mechanism of particle reacceleration to explain the flat F_ν spectra of different sources. Besides GRBs discussed in earlier studies (Xu & Zhang 2017; Xu et al. 2018) and PWNe considered here, it can also be applicable to, e.g., radio galaxies and blazars, which will be investigated in our future work.

5. Summary

Recent advances in the theoretical understanding of MHD turbulence bring us new insights in basic physical processes related to PWNe.

We suggested that the magnetic reconnection in the PW inevitably falls in the turbulent reconnection regime and thus is efficient in converting the magnetic energy to the particle energy.

We focused on the reacceleration of particles in the PWN through the mechanism ASA. The ASA acts to flatten the injected energy spectrum of electrons. It results in a flat radio spectrum (in F_ν) of the photons radiated downstream of the termination shock. The steeper X-ray spectrum can be simply attributed to synchrotron cooling, which is dominant at high energies. At intermediate energies, the detailed spectral shape depends on the acceleration timescale of the ASA.

Our analytical spectral shapes incorporating both the ASA and synchrotron cooling generally agree well with the observed broadband synchrotron spectra of PWNe. The spectral breaks can be used to constrain the acceleration timescale of the ASA and the magnetic field strength in the PWN (see Figure 5). They can also provide valuable information on the cooling time and injected electron energy (see Table 1).

S.X. acknowledges the support for Program number HST-HF2-51400.001-A provided by NASA through a grant from the Space Telescope Science Institute, which is operated by the Association of Universities for Research in Astronomy, Incorporated, under NASA contract NAS5-26555. For N.K. and O.K. the support for this work was provided by the National Aeronautics and Space Administration through the *Chandra* awards G03-14082A and TM8-19005B issued by the *Chandra X-ray Observatory* Center, which is operated by the Smithsonian Astrophysical Observatory for and on behalf of the National Aeronautics Space Administration under contract NAS8-03060. B.Z. acknowledges the NASA grant NNX15AK85G.

ORCID iDs

Siyao Xu https://orcid.org/0000-0002-0458-7828
Noel Klingler https://orcid.org/0000-0002-7465-0941
Oleg Kargaltsev https://orcid.org/0000-0002-6447-4251
Bing Zhang https://orcid.org/0000-0002-9725-2524

References

Abdo, A. A., Ackermann, M., Ajello, M., et al. 2011, Sci, 331, 739
Armstrong, J. W., Rickett, B. J., & Spangler, S. R. 1995, ApJ, 443, 209

Arons, J. 2002, in ASP Conf. Ser. 271, Neutron Stars in Supernova Remnants, ed. P. O. Slane & B. M. Gaensler (San Francisco, CA: ASP), 71
Band, D., Matteson, J., Ford, L., et al. 1993, ApJ, 413, 281
Begelman, M. C. 1998, ApJ, 493, 291
Begelman, M. C., & Li, Z.-Y. 1992, ApJ, 397, 187
Bogovalov, S. V., Chechetkin, V. M., Koldoba, A. V., & Ustyugova, G. V. 2005, MNRAS, 358, 705
Brunetti, G., & Lazarian, A. 2007, MNRAS, 378, 245
Brunetti, G., & Lazarian, A. 2016, MNRAS, 458, 2584
Chandran, B. D. G. 2000, PhRvL, 85, 4656
Chen, Y., Wang, Q. D., Gotthelf, E. V., et al. 2006, ApJ, 651, 237
Chepurnov, A., & Lazarian, A. 2010, ApJ, 710, 853
Chevalier, R. A. 2005, ApJ, 619, 839
Chevalier, R. A., & Gull, T. R. 1975, ApJ, 200, 399
Cho, J., & Lazarian, A. 2002, PhRvL, 88, 245001
Cho, J., & Lazarian, A. 2003, MNRAS, 345, 325
Coroniti, F. V. 1990, ApJ, 349, 538
Dahlin, J. T., Drake, J. F., & Swisdak, M. 2017, PhPl, 24, 092110
de Gouveia dal Pino, E. M., & Lazarian, A. 2005, A&A, 441, 845
del Valle, M. V., de Gouveia Dal Pino, E. M., & Kowal, G. 2016, MNRAS, 463, 4331
Del Zanna, L., Papini, E., Landi, S., Bugli, M., & Bucciantini, N. 2016, MNRAS, 460, 3753
Deng, W., Li, H., Zhang, B., & Li, S. 2015, ApJ, 805, 163
Dubner, G., Giacani, E., & Decourchelle, A. 2008, A&A, 487, 1033
East, W. E., Zrake, J., Yuan, Y., & Blandford, R. D. 2015, PhRvL, 115, 095002
Fleishman, G. D., & Bietenholz, M. F. 2007, MNRAS, 376, 625
Gaensler, B. M., & Slane, P. O. 2006, ARA&A, 44, 17
Giacalone, J., & Jokipii, J. R. 1999, ApJ, 520, 204
Giacalone, J., & Jokipii, J. R. 2007, ApJL, 663, L41
Goldreich, P., & Sridhar, S. 1995, ApJ, 438, 763
Guo, X., Mao, J., & Wang, J. 2017, ApJ, 843, 23
Kaplan, S. A., & Pikelner, S. B. 1970, The Interstellar Medium (Cambridge: Harvard Univ. Press)
Kardashev, N. S. 1962, AZh, 39, 393
Kennel, C. F., & Coroniti, F. V. 1984, ApJ, 283, 694
Klingler, N., Kargaltsev, O., Pavlov, G. G., et al. 2018, ApJ, 861, 5
Komissarov, S. S., & Lyubarsky, Y. E. 2004, MNRAS, 349, 779
Kowal, G., de Gouveia Dal Pino, E. M., & Lazarian, A. 2011, ApJ, 735, 102
Kowal, G., de Gouveia Dal Pino, E. M., & Lazarian, A. 2012, PhRvL, 108, 241102
Kowal, G., Falceta-Gonçalves, D. A., Lazarian, A., & Vishniac, E. T. 2017, ApJ, 838, 91
Kowal, G., & Lazarian, A. 2010, ApJ, 720, 742
Kowal, G., Lazarian, A., Vishniac, E. T., & Otmianowska-Mazur, K. 2009, RMxAC, 36, 89
Lazarian, A., & Vishniac, E. T. 1999, ApJ, 517, 700
Lazarian, A., Zhang, B., & Xu, S. 2018, arXiv:1801.04061
Lynn, J. W., Parrish, I. J., Quataert, E., & Chandran, B. D. G. 2012, ApJ, 758, 78
Lyubarsky, Y., & Kirk, J. G. 2001, ApJ, 547, 437
Ma, Y. K., Ng, C.-Y., Bucciantini, N., et al. 2016, ApJ, 820, 100
Maron, J., & Goldreich, P. 2001, ApJ, 554, 1175
Melrose, D. B. 1969, Ap&SS, 5, 131
Meszaros, P., & Rees, M. J. 1993, ApJL, 418, L59
Mignone, A., Striani, E., Tavani, M., & Ferrari, A. 2013, MNRAS, 436, 1102
Mizuno, Y., Lyubarsky, Y., Nishikawa, K.-I., & Hardee, P. E. 2011, ApJ, 728, 90
Moran, P., Shearer, A., Mignani, R. P., et al. 2013, MNRAS, 433, 2564
Olmi, B., Del Zanna, L., Amato, E., Bandiera, R., & Bucciantini, N. 2014, MNRAS, 438, 1518
Olmi, B., Del Zanna, L., Amato, E., Bucciantini, N., & Mignone, A. 2016, JPlPh, 82, 635820601
Parker, E. N. 1957, JGR, 62, 509
Pavlov, G. G., Teter, M. A., Kargaltsev, O., & Sanwal, D. 2003, ApJ, 591, 1157
Pohl, M., Yan, H., & Lazarian, A. 2005, ApJL, 626, L101
Porth, O., Komissarov, S. S., & Keppens, R. 2014a, MNRAS, 443, 547
Porth, O., Komissarov, S. S., & Keppens, R. 2014b, MNRAS, 438, 278
Preece, R. D., Briggs, M. S., Mallozzi, R. S., et al. 2000, ApJS, 126, 19
Rees, M. J., & Gunn, J. E. 1974, MNRAS, 167, 1
Reynolds, S. P., & Aller, H. D. 1988, ApJ, 327, 845
Reynolds, S. P., Pavlov, G. G., Kargaltsev, O., et al. 2017, SSRv, 207, 175
Rybicki, G. B., & Lightman, A. P. 1979, Radiative Processes in Astrophysics (New York: Wiley-Interscience)
Safi-Harb, S., Harrus, I. M., Petre, R., et al. 2001, ApJ, 561, 308
Salter, C. J., Reynolds, S. P., Hogg, D. E., Payne, J. M., & Rhodes, P. J. 1989, ApJ, 338, 171
Sari, R., Piran, T., & Narayan, R. 1998, ApJL, 497, L17
Sironi, L., & Spitkovsky, A. 2011, ApJ, 741, 39
Slane, P., Helfand, D. J., Reynolds, S. P., et al. 2008, ApJL, 676, L33
Sweet, P. A. 1958, in IAU Symp. 6, Electromagnetic Phenomena in Cosmical Plasma, ed. B. Lehnert (New York: Cambridge Univ. Press), 123
Takamoto, M., Inoue, T., & Lazarian, A. 2015, ApJ, 815, 16
Tanaka, S. J., & Asano, K. 2017, ApJ, 841, 78
Tanaka, S. J., Takahara, F., Bulgarelli, A., & Vittorini, V. 2011, ApJ, 741, 40
Tavani, M., Bulgarelli, A., Vittorini, V., et al. 2011, Sci, 331, 736
Wang, Q. D., Gotthelf, E. V., Chu, Y.-H., & Dickel, J. R. 2001, ApJ, 559, 275
Weibel, E. S. 1959, PhRvL, 2, 83
Wilms, J., Allen, A., & McCray, R. 2000, ApJ, 542, 914
Xu, S., & Lazarian, A. 2016, ApJ, 833, 215
Xu, S., & Lazarian, A. 2018, ApJ, 868, 36
Xu, S., Yan, H., & Lazarian, A. 2016, ApJ, 826, 166
Xu, S., Yang, Y.-P., & Zhang, B. 2018, ApJ, 853, 43
Xu, S., & Zhang, B. 2017, ApJL, 846, L28
Yan, H., & Lazarian, A. 2002, PhRvL, 89, B1102
Yan, H., & Lazarian, A. 2004, ApJ, 614, 757
Yan, H., & Lazarian, A. 2008, ApJ, 673, 942
Yan, H., Lazarian, A., & Petrosian, V. 2008, ApJ, 684, 1461
Yusef-Zadeh, F., & Gaensler, B. M. 2005, AdSpR, 35, 1129
Zhang, B., & Yan, H. 2011, ApJ, 726, 90
Zhu, B.-T., Zhang, L., & Fang, J. 2018, A&A, 609, A110
Zrake, J. 2016, ApJ, 823, 39
Zrake, J., & East, W. E. 2016, ApJ, 817, 89